Research Article

Structure-Enhanced Mechanically Robust Graphite Foam with Ultrahigh MnO$_2$ Loading for Supercapacitors

Qinghe Cao,[1] Junjie Du,[1] Xiaowan Tang,[1] Xi Xu ⓘ,[2] Longsheng Huang,[3] Dongming Cai,[3] Xu Long ⓘ,[4] Xuewen Wang,[1] Jun Ding,[2] Cao Guan ⓘ,[1] and Wei Huang ⓘ[1]

[1]*Frontiers Science Center for Flexible Electronics, Institute of Flexible Electronics, Northwestern Polytechnical University, Xi'an 710072, China*

[2]*Department of Materials Science and Engineering, National University of Singapore, 9 Engineering Drive 1, Singapore, Singapore 117576*

[3]*College of Chemical Engineering, Hubei University, Wuhan 430062, China*

[4]*School of Mechanics, Civil Engineering and Architecture, Northwestern Polytechnical University, Xi'an 710072, China*

Correspondence should be addressed to Xi Xu; xu_xi@u.nus.edu, Cao Guan; iamcguan@nwpu.edu.cn, and Wei Huang; iamwhuang@nwpu.edu.cn

With the fast bloom of flexible electronics and green vehicles, it is vitally important to rationally design and facilely construct customized functional materials with excellent mechanical properties as well as high electrochemical performance. Herein, by utilizing two modern industrial techniques, digital light processing (DLP) and chemical vapor deposition (CVD), a unique 3D hollow graphite foam (HGF) is demonstrated, which shows a periodic porous structure and robust mechanical properties. Finite element analysis (FEA) results confirm that the properly designed gyroidal porous structure provides a uniform stress area and mitigates potential structural failure caused by stress concentrations. A typical HGF can show a high Young's modulus of 3.18 MPa at a low density of 48.2 mg cm^{-3}. The porous HGF is further covered by active MnO$_2$ material with a high mass loading of 28.2 mg cm^{-2} (141 mg cm^{-3}), and the MnO$_2$/HGF electrode still achieves a satisfactory specific capacitance of 260 F g^{-1}, corresponding to a high areal capacitance of 7.35 F cm^{-2} and a high volumetric capacitance of 36.75 F cm^{-3}. Furthermore, the assembled quasi-solid-state asymmetric supercapacitor also shows remarkable mechanical properties as well as electrochemical performance.

1. Introduction

The growing requirement for energy in electronics as well as vehicles has prompted extensive researches on the development of high-performance energy storage devices with higher energy densities and power densities [1–4]. Increasing the mass loading (larger than 10 mg cm^{-2}) for commercially available electrodes often leads to the decline of utilization efficiency of the active materials due to sluggish ion/electron transport in bulk reactions [5–11]. Design of a 3D structured electrode containing interconnected porous network can ensure efficient charge transport throughout the entire electrode, which is necessary for the utilization of all active materials and the realization of high rate capability with high capacity/capacitance. With the fast development of 3D print-

ing technology, it has been widely utilized for the construction of functional materials with unique predesigned structures for efficient energy storage devices [12–19]. For example, 3D graphene/graphite-based materials have been widely studied for high-performance energy storage devices due to their low density, high conductivity, and excellent electrochemical stability [20–24]. However, most of the previous studies on 3D printed electrode materials were focused on extrusion-based techniques, where the resolution is low (usually larger than 200 μm) and only certain simple 3D structures (like lattices and interdigitated structure) can be achieved. In addition, the mechanical properties of such 3D carbon materials, which are essential for packaging, transportation, and utilization, are also important for the realization of high-performance energy storage devices, but they
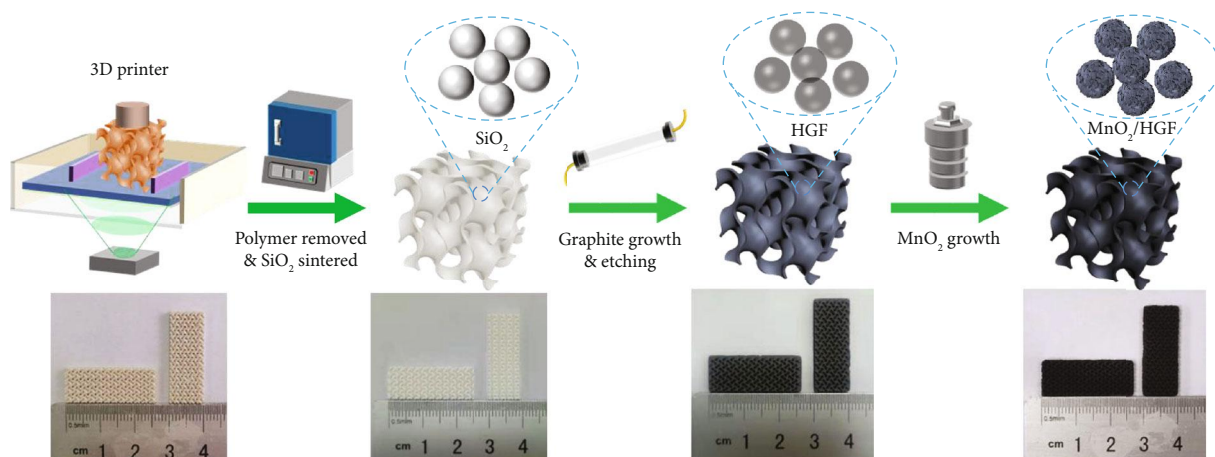
FIGURE 1: Schematic illustration of the fabrication process of the MnO$_2$/HGF electrode.

were merely discussed in previous reports [11, 15, 18, 24–27]. With the above concern, it will be very promising to develop novel 3D printed electrodes with higher resolution and unique structure design, which will bring about promising mechanical properties and electrochemical performance.

In this work, an ultralight and ultrastiff HGF with a gyroid structure is prepared though integrating DLP technology with the CVD method. Different from extrusion-based 3D printing, DLP technology is based on a fast photopolymerization process where few structural supports are required; thus, various complex 3D architectures with high resolution can be achieved [28–31]. The selected gyroid structure has been reported with high stiffness at low density, but it is hard to construct it with extrusion-based methods [24, 26]. FEA results confirm that the gyroid HGF can provide a uniform stress distribution, thereby mitigating early structural failure caused by stress concentrations. The final HGF can show a high Young's modulus of 3.18 MPa at the low density of 48.2 mg cm^{-3} in compressive performance tests. In addition to the mechanical robustness, the HGF electrode with well-designed hierarchical porosity also can deliver a high mass loading of MnO$_2$ with superior electrochemical performance. MnO$_2$/HGF with a high mass loading of 28.2 mg cm^{-2} (141 mg cm^{-3}) achieves a high areal capacitance of 7.35 F cm^{-2} and a high volumetric capacitance of 36.75 F cm^{-3} with a specific capacitance of 260 F g^{-1}. Further assembled HFG-based quasi-solid-state asymmetric supercapacitor also exhibits a remarkable energy density of 0.96 mWh cm^{-2} under a power density of 50 mW cm^{-2} as well as excellent mechanical stability. The 3D HGF with hierarchical porous structure and robust mechanical properties, the customizable facile fabrication process using 3D printing and CVD, together with the promising mechanical and electrochemical properties would pave a good way for the development of high-performance energy storage devices.

2. Results

2.1. Fabrication of MnO$_2$/HGF Electrode. The schematic fabrication process of the MnO$_2$/HGF electrode with the photographs of the samples at each step is shown in Figure 1 (more

details are in the Supplementary Materials (available here)). A gyroid SiO$_2$ template was firstly designed by computer software and prepared by the high-resolution DLP technology with photopolymerization of UV-curable resin mixed with SiO$_2$ microspheres. After 3D printing, a debinding and sintering process was further conducted, in which the photopolymer was completely removed and SiO$_2$ was molded. Then, a graphite layer was deposited on the surface of the SiO$_2$ template by the CVD method (the experimental setup and reaction route diagram are shown in Figure S1), where the densities and mechanical properties of the graphite can be simply controlled by the deposition time. After etching away the SiO$_2$ by aqueous HF solution, MnO$_2$ nanosheet arrays were further grown on the surface of HGF, resulting in a hybrid electrode of MnO$_2$/HGF.

2.2. The Mechanical Properties of HGF. FEA is performed to evaluate the influences of the structure for HGF on their mechanical properties (Figure 2(a)). For comparison, three shell structures including lattice, primitive, and gyroid were modeled and analyzed, and their volume ($2 \times 2 \times 1$ mm^3) and thickness (0.1 mm) are fixed consistently. (Red color highlights the stress concentration area. According to the barrel principle, the fracture of these stress concentration points will lead to the destruction of the overall structure.) As indicated from the color distribution, the gyroid structure can provide a uniform stress area with no significant red part. This can be attributed to the continuous periodic structure that can relive stress well, thus effectively avoiding the possible collapse caused by the localized stress concentration. As a comparison, multiple stress concentration points appeared at the connection parts for lattice structure and the neck regions for primitive structure, indicating poor mechanical stability.

In order to further explore the mechanical properties, a gyroidal HGF with an ultralow density of 48.2 mg cm^{-3} was prepared. As demonstrated in Figure 2(b), the HGF with a volume of $2.7 * 1 * 0.2$ cm^3 can steadily stand on a dandelion flower without causing any deformation. More important, the ultralight HGF can withstand 15000 times its own weight without obvious degradation (Figure 2(c)). To further confirm, a compressive test is carried out and the stress-strain
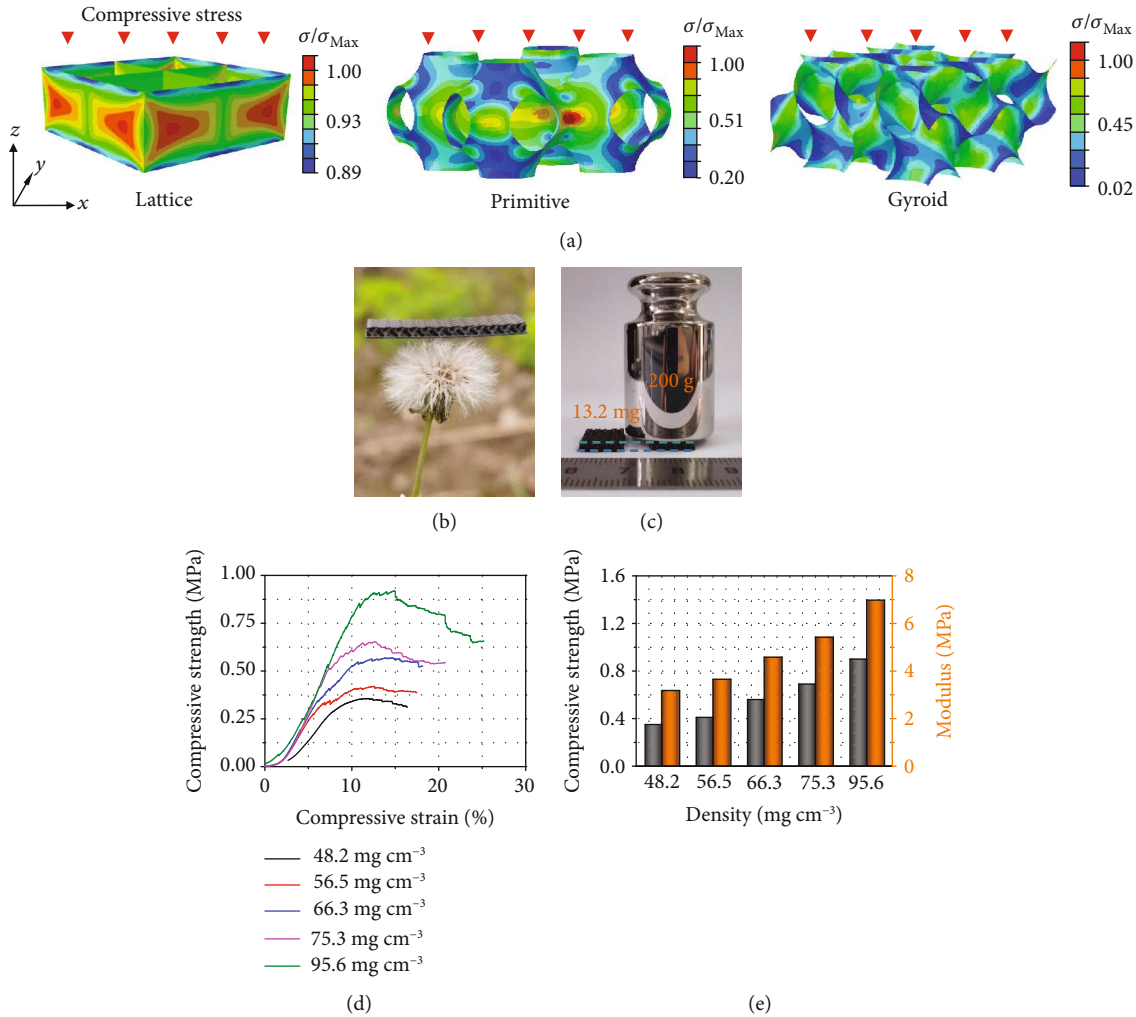
(a)

(b)

(c)

(d)

(e)

FIGURE 2: Mechanical properties of HGF. (a) FEA models of lattice, primitive, and gyroid structures and their stress distributions under the same compressive strain along the z-direction (the values of σ_{Max} for lattice, primitive, and gyroid structure are 600 MPa, 770 MPa and 600 MPa, respectively). (b) Ultralight and (c) Ultrastiff properties illustrated by the gyroidal HGF. (d) Compressive stress-strain curves of HGF with different densities. (e) Compressive strength and Young's modulus of HGF with different densities.

responses with different densities under compressive load are recorded in Figure 2(d). A high compressive pressure of 0.35 MPa can be achieved for HGF at a low density of 48.2 mg cm^{-3}, and the value increased to 0.9 MPa with a higher density of 95.6 mg cm^{-3}. Young's modulus, which can reveal the ability of resisting deformation, is calculated and shown in Figure 2(e). The high values of 3.18 MPa at $\rho = 48.2$ mg cm^{-3} and 6.98 MPa at $\rho = 95.6$ mg cm^{-3} confirm the high stiffness of HGF, which also stands out from many other carbon-based porous materials, such as graphene-carbon aerogels [32], BC-LRF carbon aerogels [33], graphene crosslinked carbon nanotube sponge/polyimide (Gw-CNT/PI) [34], and carbonaceous aerogels [35]. The FEA and compressive results indicate that the gyroidal HGF can well integrate porous, lightweight properties with promising mechanical stiffness.

2.3. Characterization of HGF and MnO$_2$/HGF. From the scanning electron microscopy (SEM) image in Figure 3(a),

the HGF can well retain the gyroid structure of the SiO$_2$ template without any collapse after acid etching, indicating good chemical and structural stability. From enlarged SEM images (Figure S2a and S2b), it can be seen that the HGF has spherical shapes on the surface, which is in accordance with the grain morphology of SiO$_2$ before carbon deposition. Transmission electron microscopy (TEM) images in Figures 3(b) and 3(c) illustrate the hollow feature of the HGF after removal of the SiO$_2$ template. Similar results can be obtained by energy-dispersive X-ray spectroscopy (EDX) mapping results (Figure 3(d) and Figure S3a). The high-resolution TEM (HRTEM) in Figure 3(e) clearly exhibits regular graphitic lattice fringes, indicating the good crystallinity of HGF. From the Raman spectra in Figure S4, an additional characteristic 2D band peak is detected from HGF (compared to the controlled samples of GO and RGO), revealing the existence of the graphene structure. The X-ray diffraction (XRD) pattern in Figure S5 shows that after acid etching, the diffraction peaks of SiO$_2$
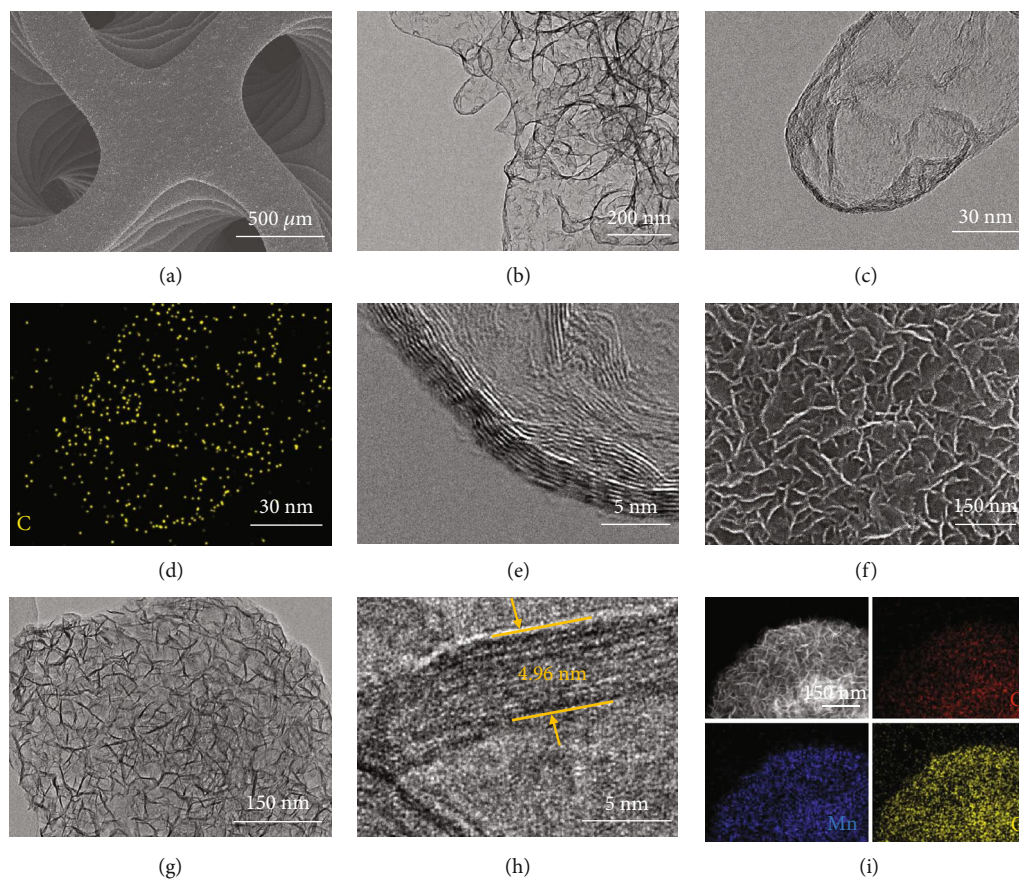
FIGURE 3: Morphology and structure of the HGF and MnO$_2$/HGF: (a) SEM, (b, c) TEM, (d) EDX mapping, and (e) HRTEM images of HGF; (f) SEM, (g) TEM, (h) HRTEM, and (i) EDX mapping images of MnO$_2$/HGF.

completely disappeared and the peaks that appeared at 26.2° and 44.3° belong to the (002) and (101) planes of graphite, respectively.

After a simple hydrothermal reaction, MnO$_2$ nanosheets (about 150 nm) are fully covered on the HGF surface (Figure 3(f) and Figure S2c-d). The nanosheets are interconnected to each other to form a network and generate a large number of micropores. Considering the continuous macropores derived by the gyroid structure and the mesopores from graphite microspheres, the MnO$_2$/HGF indeed displays hierarchical porosity. Such a hierarchical porous structure provides more accessible surfaces for the electrode-electrolyte contact and reduces the resistance for ion/electron transport. TEM images of MnO$_2$/HGF in Figure 3(g) further prove that MnO$_2$ nanosheets are uniformly distributed on the HGF surface. From the HRTEM (Figure 3(h)), it can be seen that a typical MnO$_2$ nanosheet presents a small sheet thickness of ~4.96 nm, which would fully expose the surface for electrochemical reaction and greatly promote the fast charge transfer within the electrode. The EDX spectrum (Figure S3b) and mapping images (Figure 3(i)) further show the homogeneous element distribution of Mn, O, and C. From the XRD spectrum in Figure S5, the additional two diffraction peaks at 37.1° and 66.7° match well with the (100) and (110) planes of ε-MnO$_2$ (PDF#30-0802), respectively.

2.4. Electrochemical Properties of MnO$_2$/HGF.

The electrochemical performance of HGF and MnO$_2$/HGF electrodes was first studied. As shown in Figure 4(a), after the loading of MnO$_2$ nanosheet arrays, the capacitance of HGF is significantly increased with a much larger enclosed area in the cyclic voltammogram (CV) curves. From Figure 4(b) and Figure S6, the bare HGF electrode shows a small capacitance (0.5 F cm^{-2}), while the MnO$_2$/HGF electrode (with 28.2 mg cm^{-2} of MnO$_2$) achieves a high areal capacitance of 7.35 F cm^{-2} at a current density of 1 mA cm^{-2}. In addition, the MnO$_2$/HGF also demonstrated an excellent high rate capability that was 77.8% of the capacitance that can be maintained when the current density increased from 1 to 20 mA cm^{-2}, suggesting highly efficient charge transfer and ion diffusion. To highlight, the MnO$_2$/HGF shows promising high mass loading with high areal capacitance, as compared with other MnO$_2$-based electrodes [36–44] (Figure 4(c)), showing its great potential for practical usage.

For further optimization, three MnO$_2$/HGF electrodes with gradient mass loadings by tuning the hydrothermal reaction time were prepared. As shown in Figure 4(d) and Figure S7, all the three samples show near-rectangular CV behaviors, indicating good reaction kinetics, and the sample with a higher MnO$_2$ loading results in a larger enclosed area. Figure 4(e) further compares the areal, volumetric, and specific capacitances of the three electrodes. The MnO$_2$/HGF electrode with 16 mg cm^{-2} of MnO$_2$ achieves
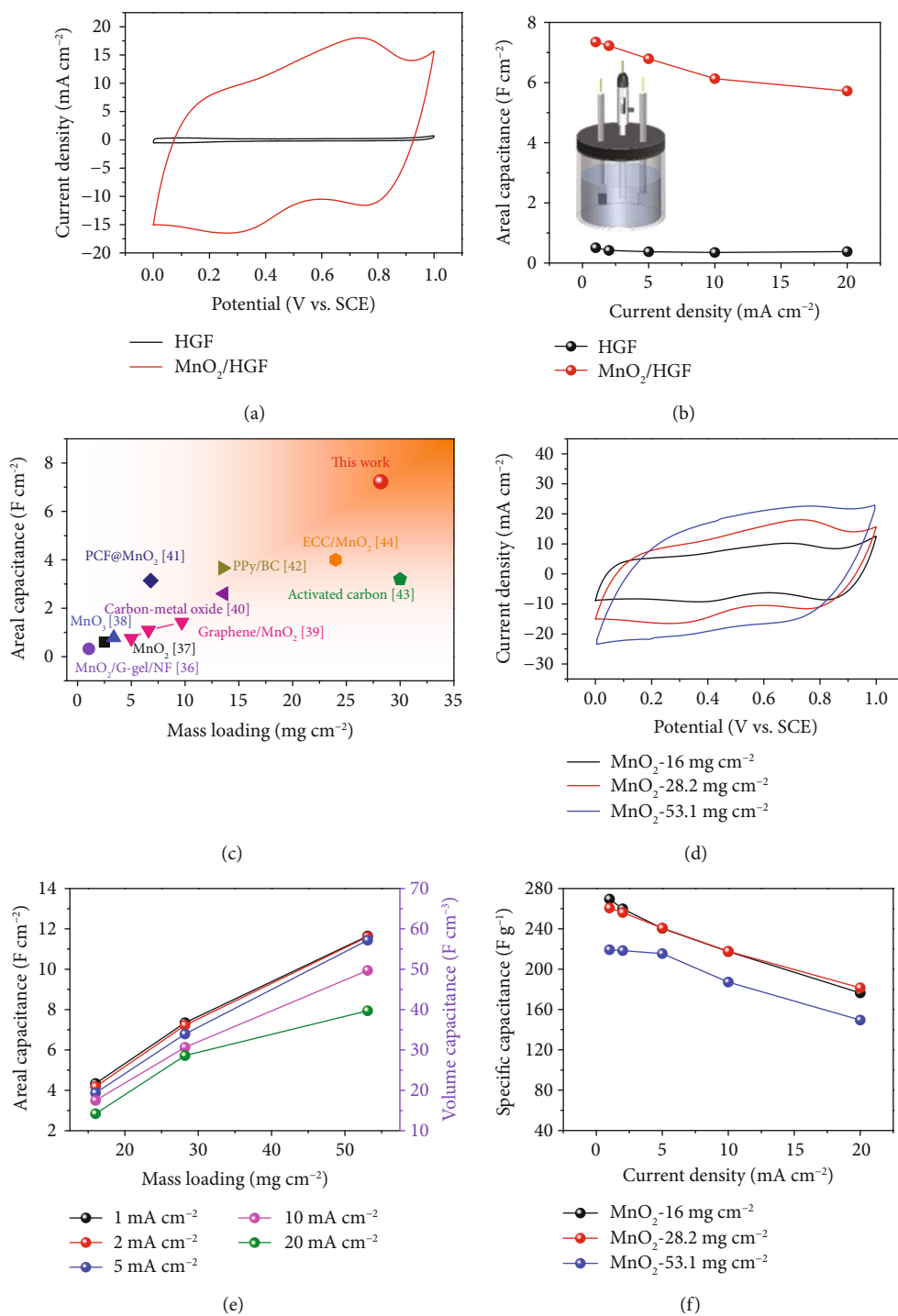
(a)

(b)

(c)

(d)
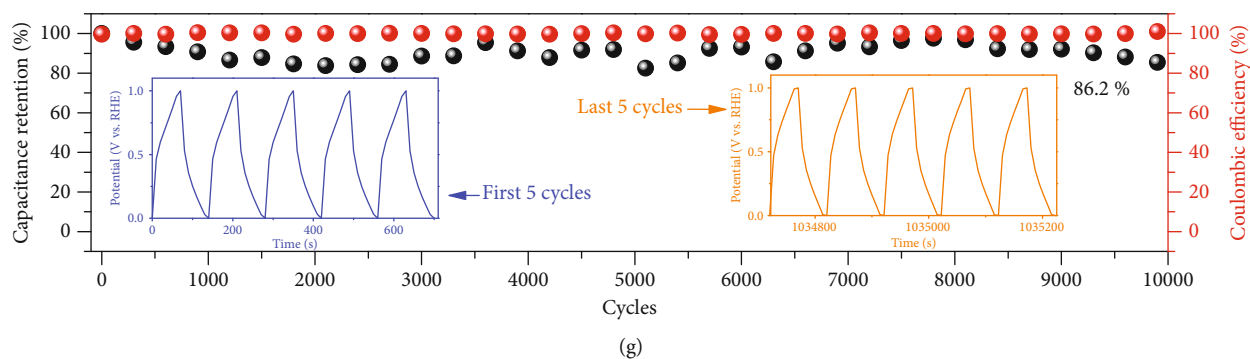

(e)

(f)

FIGURE 4: Continued.

FIGURE 4: Electrochemical characterizations of MnO$_2$/HGF. (a) CV curves and (b) areal capacitances of HGF and MnO$_2$/HGF. (c) Comparison of areal capacitance and loading mass of MnO$_2$/HGF with those of previously reported MnO$_2$-based electrodes. (d) CV curves of MnO$_2$/HGF with different mass loadings of MnO$_2$. (e) Areal capacitances and volumetric capacitances and (f) specific capacitances obtained from MnO$_2$/HGF with different mass loadings of MnO$_2$ at different current densities. (g) Cycling performance of MnO$_2$/HGF at a current density of 50 mA cm^{-2}.

areal and volumetric capacitances of 4.3 F cm^{-2} and 21.5 F cm^{-3}, and the values increase almost linearly to 11.6 F cm^{-2} and 58.2 F cm^{-3}, respectively, when the MnO$_2$ loading is 53.1 mg cm^{-2}. The MnO$_2$/HGF electrode with a high MnO$_2$ mass loading of 53.1 mg cm^{-2} still maintains 68.2% of the initial capacitance when the current density increased from 1 to 20 mA cm^{-2}, demonstrating a superior rate capability. Such observation further proves that the predesigned hierarchical porous carbon structure possesses a large ion/electron accessible area and is beneficial to the rapid charge transfer. In Figure 4(f), it can be seen that the MnO$_2$/HGF electrode with 16 mg cm^{-2} of MnO$_2$ exhibits a specific capacitance of 269 F g^{-1}, and the value decreases slightly to 260 F g^{-1} when the loading mass of MnO$_2$ increases to 28.2 mg cm^{-2}. Even when MnO$_2$ reaches 53.1 mg cm^{-2}, the MnO$_2$/HGF electrode still achieves a satisfactory specific capacitance of 219.3 F g^{-1}. To highlight, the high mass loadings together with the high areal/specific capacitances illustrated by the MnO$_2$/HGF compare favorably with the values reported from many other MnO$_2$-based electrodes (Table S1) [41, 44, 45]. The obtained electrochemical performance of MnO$_2$/HGF can be the result from the gyroid hierarchical porous structure that is beneficial to the transfer of ions/electrons between the electrode and the electrolyte and the well-conducting graphitic carbon with thin-layered MnO$_2$ that effectively enhances the reaction kinetics.

The structural merits of HGF are further studied by comparing it with a commonly used carbon cloth (CC) substrate which is highly conductive but has limited porosity (Figure S8). The MnO$_2$/CC electrode was prepared using the CC substrate with the same hydrothermal method as MnO$_2$/HGF. The mass loading of MnO$_2$ can only reach 1.8 mg in MnO$_2$/CC, which is only 1/16 of that for MnO$_2$/HGF (the thickness of CC is 1/3 of HGF). In addition, the specific capacitance and rate capability of MnO$_2$/CC are both poorer than those of MnO$_2$/HGF, showing the potential usage of HGF for energy storage devices.

The MnO$_2$/HGF electrode with 28.2 mg cm^{-2} of MnO$_2$ was further applied for the stability test. As shown in

Figure 4(g), at the fixed charge/discharge current density of 50 mA cm^{-2}, the MnO$_2$/HGF electrode can maintain 86.2% of the initial capacitance after 10000 cycles, demonstrating good cycle stability. SEM images after the cycling test (Figure S9) display the well-maintained structure of MnO$_2$/HGF, further confirming the good cycling stability.

2.5. HGF-Based Asymmetric Supercapacitor. To prove the practical applications of porous HGF, the negative electrode of polypyrrole/N-doped carbon/HGF (noted as PPy-NC/HGF) is further prepared by electrodepositing PPy on a NC array-coated HGF (Figure S10-12) [46, 47], and an asymmetric supercapacitor based on MnO$_2$/HGF and PPy-NC/HGF is assembled (noted as MnO$_2$/HGF//PPy-NC/HGF).

The CV curves of the MnO$_2$/HGF and PPy-NC/HGF, with a respective potential window of 0 to 1 V and −1 to 0 V, are shown in Figure S13a. The two electrodes can be well-matched with similar capacitance. The CV curves (Figure S13b) of the assembled MnO$_2$/HGF//PPy-NC/HGF aqueous supercapacitor show an overall voltage of 0–2 V with good capacitive behavior. As shown in Figure S13c, the GCD curves at various current densities were further evaluated, and an impressive areal capacitance of 2.8 F cm^{-2} is achieved at a current density of 1 mA cm^{-2}. When the current density increases to 20 mA cm^{-2}, 75% of the value (F cm^{-2}) can remain unchanged, indicating the excellent rate capability (Figure S13d). The EIS result (inset in Figure S13d) shows that the aqueous asymmetric supercapacitor possesses small charge transfer resistance and ion diffusion resistance, revealing good electronic conductivity. Two asymmetric supercapacitors connected in series can power sixteen green LEDs and ten blue LEDs (Figure S13e). The MnO$_2$/HGF//PPy-NC/HGF also shows good cycling stability (Figure S13e) that 77.7% of the initial capacitance is maintained after 10000 cycles.

A quasi-solid-state asymmetric supercapacitor was also assembled using MnO$_2$/HGF and PPy-NC/HGF electrodes with a gel electrolyte, as schematically presented in Figure 5(a). The quasi-solid-state supercapacitor exhibits near-rectangular CV curves with a voltage window of 2 V (Figure 5(b)). Based on the GCD curves (Figure S13f), the
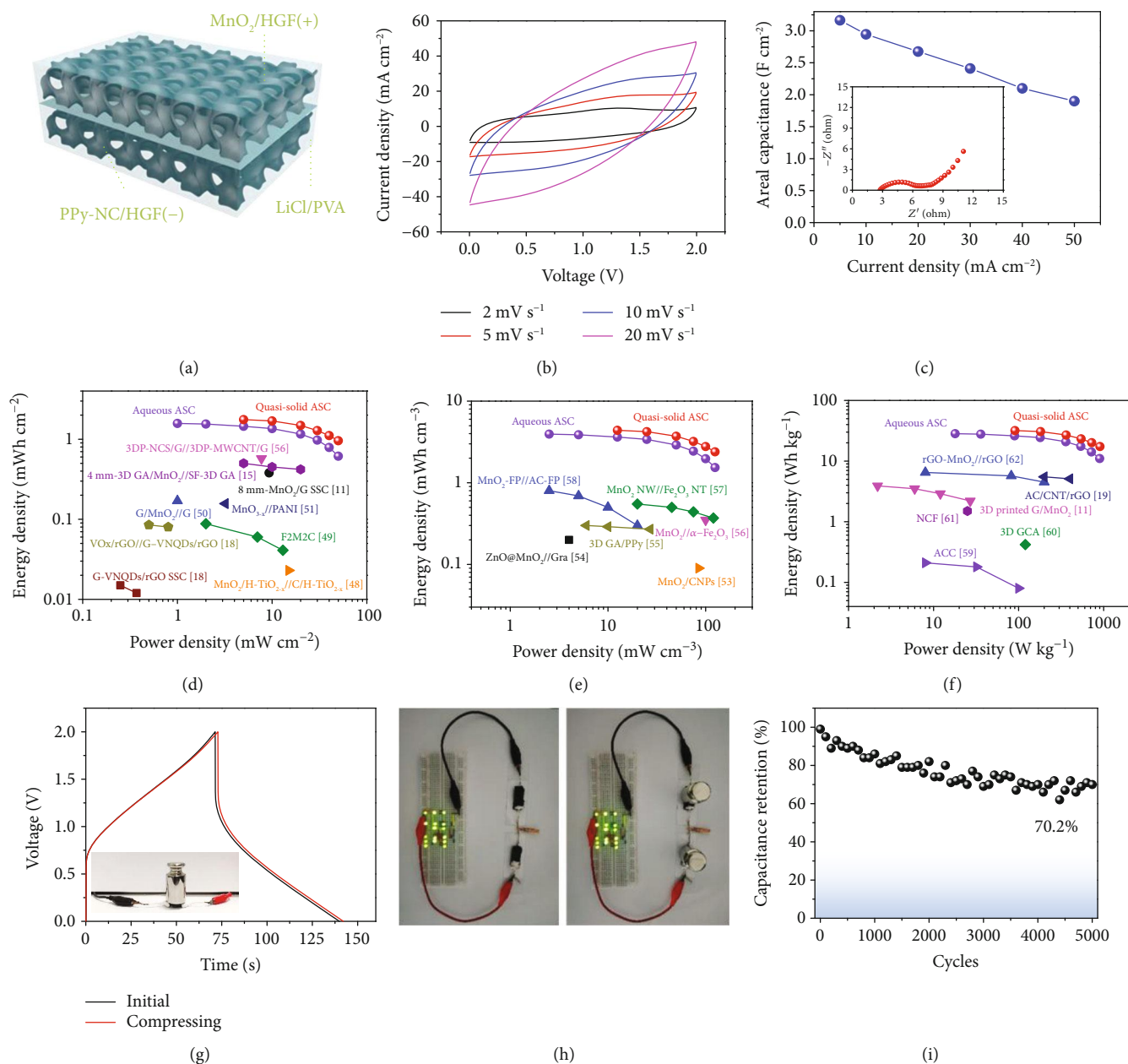
FIGURE 5: Electrochemical properties of the HFG-based quasi-solid-state supercapacitor. (a) Schematic structure, (b) CV curves, and (c) areal capacitances of the HGF-based asymmetric supercapacitor. Inset in (c) is the EIS results. Ragone plots of aqueous and quasi-solid-state asymmetric supercapacitor based on (d) area, (e) volume, and (f) active material mass of the whole device. (g) Comparison of the CV curves of the asymmetric supercapacitor in its initial state and under compression. (h) Photographs of LEDs powered by two HGF-based supercapacitors in the initial state and under compression. (i) Cycling performance of the HGF-based asymmetric supercapacitor.

quasi-solid-state cell achieves an areal capacitance of $3.165\,F\,cm^{-2}$ at a current density of $5\,mA\,cm^{-2}$ and maintains $1.9\,F\,cm^{-2}$ at a current density of $50\,mA\,cm^{-2}$, presenting a satisfactory rate capability (Figure 5(c)). Besides, the EIS results (inset of Figure 5(c)) indicate that the quasi-solid-state supercapacitor has small resistance for ion transfer. The areal energy density and high power density of the quasi-solid-state cell are exhibited in Figure 5(d). The $MnO_2/HGF//PPy-NC/HGF$ cell achieves a high areal energy density of $1.76\,mWh\,cm^{-2}$ at a power density of $5\,mW\,cm^{-2}$, and maintains $0.96\,mWh\,cm^{-2}$ at

$50\,mW\,cm^{-2}$, which are much higher than the other documented works on MnO_2-based supercapacitors, showing the great promise of the porous HGF (Table S2) [11, 15, 18, 48–52]. The supercapacitor also exhibits a volumetric energy density of $3.94\,mWh\,cm^{-3}$ at a power density of $2.5\,mW\,cm^{-3}$ and retains $1.54\,mWh\,cm^{-3}$ at a high power density of $125\,mW\,cm^{-3}$ (Figure 5(e)). In addition, it can achieve a specific energy density of $31.9\,Wh\,kg^{-1}$ at a power density of $90.6\,W\,kg^{-1}$ and reaches a high power density of $905.8\,W\,kg^{-1}$ at an energy density of $17.4\,Wh\,kg^{-1}$ (Figure 5(f)). These values are also better than

many previously reported supercapacitors, where the mass loadings are much smaller [11, 19, 53–62].

To further reveal the mechanical robustness of the HGF-based device for practical usage, the GCD curves of the cell in the initial state and under compression were recorded. As shown in Figure 5(g), there is only a slight shift in the GCD curves, indicating its excellent stability under mechanical pressure. One step further, two quasi-solid-state cells connected in series were used to light up 16 green LEDs (Figure 5(h) and Movie 1), and the brightness of the LEDs remains unchanged after the cells are pressed with a heavy counterweight. The quasi-solid-state device also maintains 70.2% of the initial capacitance after 5000 cycles, showing good cycling stability (Figure 5(i)).

3. Conclusion

In conclusion, a porous and robust HGF with lightweight has been rationally designed and facilely constructed with the help of DLP and CVD. FEA calculation and compression tests prove that the porous HGF with a gyroidal porous structure can effectively prevent structural failure from stress concentrations thus maintaining mechanical robustness. The graphite foam was further coated with MnO_2 nanosheets, which can be directly utilized as electrode materials for supercapacitors, without using additional binders and current collectors. Due to the unique hollow and porous structure, not only a high mass loading of active materials can be achieved, the electrode also demonstrated remarkably high areal and volumetric capacitances. A quasi-solid-state asymmetric supercapacitor is further assembled and shows outstanding electrochemical properties as well as excellent mechanical performance. Such a strategy for 3D porous and robust materials with promising mechanical and electrochemical properties would pave a good way for the practical applications of advanced energy storage devices.

4. Materials and Methods

The experimental procedure including the preparation of HGF, fabrication of MnO_2/HGF and PPy-NC/HGF, FEA calculation, characterizations, and electrochemical measurement can be found in the Supplementary Materials.

Conflicts of Interest

The authors declare no conflict of interest.

Authors' Contributions

Qinghe Cao and Junjie Du contributed equally to this work. Qinghe Cao, Junjie Du, and Xi Xu conducted the material fabrication. Qinghe Cao, Junjie Du, Xi Xu, Longsheng Huang, Dongming Cai, and Xuewen Wang provided material characterizations. Qinghe Cao and Junjie Du conducted the electrochemical test. Xiaowan Tang and Xu Long did the FEA calculation. Jun Ding, Cao Guan, and Wei Huang supervised the project.

Supplementary Materials

Figure S1: scheme of experimental setup and reaction route diagram in CVD process. Figure S2: SEM images of HGF and MnO_2/HGF. Figure S3: EDS of HGF and MnO_2/HGF. Figure S4: Raman spectra of HGF, rGO, and GO. Figure S5: XRD of HGF/SiO_2, HGF, and MnO_2/HGF. Figure S6: electrochemical performance of HGF and MnO_2/HGF. Figure S7: electrochemical performance of MnO_2/HGF electrodes with different mass loadings. Figure S8: electrochemical performance of MnO_2/CC. Figure S9: SEM images of MnO_2/HGF after 10000-cycle test. Figure S10: SEM images of Co-NC/HGF, NC/HGF, and PPy-NC/HGF and TEM images of PPy-NC/HGF. Figure S11: XRD and Raman spectra of PPy-NC/HGF. Figure S12: electrochemical performance of PPy-NC/HGF. Figure S13: electrochemical performance of aqueous asymmetric supercapacitor. Table S1: summary of the areal capacitance, specific capacitance, and rate capability of electrodes with high mass loading of MnO_2. Table S2: summary of voltage window, capacitance, and areal energy density (power density) of current study with other reported aqueous and quasi-solid-state devices. *(Supplementary Materials)*

References

[1] M. P. Browne, E. Redondo, and M. Pumera, "3D printing for electrochemical energy applications," *Chemical Reviews*, vol. 120, no. 5, pp. 2783–2810, 2020.

[2] Z. Qi and H. Wang, "Advanced thin film cathodes for lithium ion batteries," *Research*, vol. 2020, article 2969510, pp. 1–24, 2020.

[3] M. Peng, D. Shi, Y. Sun et al., "3D printed mechanically robust graphene/CNT electrodes for highly efficient overall water splitting," *Advanced Materials*, vol. 32, no. 23, article e1908201, 2020.

[4] H. Bi, T. Lin, F. Xu, Y. Tang, Z. Liu, and F. Huang, "New graphene form of nanoporous monolith for excellent energy storage," *Nano Letters*, vol. 16, no. 1, pp. 349–354, 2016.

[5] Y. Li, J. Henzie, T. Park et al., "Fabrication of flexible microsupercapacitors with binder-free ZIF-8 derived carbon films via electrophoretic deposition," *Bulletin of the Chemical Society of Japan*, vol. 93, no. 1, pp. 176–181, 2020.

[6] S. Makino, Y. Yamauchi, and W. Sugimoto, "Synthesis of electro-deposited ordered mesoporous RuOx using lyotropic liquid crystal and application toward micro-supercapacitors," *Journal of Power Sources*, vol. 227, pp. 153–160, 2013.

[7] N. L. Wulan Septiani, Y. V. Kaneti, K. B. Fathoni et al., "Self-assembly of nickel phosphate-based nanotubes into two-dimensional crumpled sheet-like architectures for high-performance asymmetric supercapacitors," *Nano Energy*, vol. 67, article 104270, 2020.

[8] J. Tang, R. R. Salunkhe, H. Zhang et al., "Bimetallic metal-organic frameworks for controlled catalytic graphitization of nanoporous carbons," *Scientific Reports*, vol. 6, no. 1, article 30295, 2016.

[9] H. Sun, J. Zhu, D. Baumann et al., "Hierarchical 3D electrodes for electrochemical energy storage," *Nature Reviews Materials*, vol. 4, no. 1, pp. 45–60, 2019.

[10] P. Chang, H. Mei, Y. Zhao, W. Huang, S. Zhou, and L. Cheng, "3D structural strengthening urchin-like $Cu(OH)_2$-based symmetric supercapacitors with adjustable capacitance," *Advanced Functional Materials*, vol. 29, no. 34, article 1903588, 2019.

[11] B. Yao, S. Chandrasekaran, J. Zhang et al., "Efficient 3D printed pseudocapacitive electrodes with ultrahigh MnO_2 loading," *Joule*, vol. 3, no. 2, pp. 459–470, 2019.

[12] N. Wei, L. Yu, Z. Sun et al., "Scalable salt-templated synthesis of nitrogen-doped graphene nanosheets toward printable energy storage," *ACS Nano*, vol. 13, no. 7, pp. 7517–7526, 2019.

[13] S. D. Lacey, D. J. Kirsch, Y. Li et al., "Extrusion-based 3D printing of hierarchically porous advanced battery electrodes," *Advanced Materials*, vol. 30, no. 12, article e1705651, 2018.

[14] M. Peng, Z. Wen, L. Xie et al., "3D printing of ultralight biomimetic hierarchical graphene materials with exceptional stiffness and resilience," *Advanced Materials*, vol. 31, no. 35, article e1902930, 2019.

[15] B. Yao, S. Chandrasekaran, H. Zhang et al., "3D-printed structure boosts the kinetics and intrinsic capacitance of pseudocapacitive graphene aerogels," *Advanced Materials*, vol. 32, no. 8, article e1906652, 2020.

[16] W. Yang, J. Yang, J. J. Byun et al., "3D printing of freestanding MXene architectures for current-collector-free supercapacitors," *Advanced Materials*, vol. 31, no. 37, article e1902725, 2019.

[17] C. Ma, R. Wang, H. Tetik et al., "Hybrid nanomanufacturing of mixed-dimensional manganese oxide/graphene aerogel macroporous hierarchy for ultralight efficient supercapacitor electrodes in self-powered ubiquitous nanosystems," *Nano Energy*, vol. 66, pp. 104124–104131, 2019.

[18] K. Shen, J. Ding, and S. Yang, "3D printing quasi-solid-state asymmetric micro-supercapacitors with ultrahigh areal energy density," *Advanced Energy Materials*, vol. 8, no. 20, article 1800408, 2018.

[19] T. Gao, Z. Zhou, J. Yu et al., "3D printing of tunable energy storage devices with both high areal and volumetric energy densities," *Advanced Energy Materials*, vol. 9, no. 8, article 1802578, 2019.

[20] P. Wu, Z. Fang, A. Zhang et al., "Chemically binding scaffolded anodes with 3D graphene architectures realizing fast and stable lithium storage," *Research*, vol. 2019, article 8393085, pp. 1–9, 2019.

[21] K. Fu, Y. Yao, J. Dai, and L. Hu, "Progress in 3D printing of carbon materials for energy-related applications," *Advanced Materials*, vol. 29, no. 9, article 1603486, 2017.

[22] X. Xu, C. Guan, L. Xu et al., "Three dimensionally free-formable graphene foam with designed structures for energy and environmental applications," *ACS Nano*, vol. 14, no. 1, pp. 937–947, 2020.

[23] Y. Wang, Q. Cao, C. Guan, and C. Cheng, "Recent advances on self-supported arrayed bifunctional oxygen electrocatalysts for flexible solid-state Zn-air batteries," *Small*, vol. 16, no. 33, article 2002902, 2020.

[24] Z. Qin, G. S. Jung, M. J. Kang, and M. J. Buehler, "The mechanics and design of a lightweight three-dimensional graphene assembly," *Science Advances*, vol. 3, no. 1, article e1601536, 2017.

[25] H. Kashani, Y. Ito, J. Han, P. Liu, and M. Chen, "Extraordinary tensile strength and ductility of scalable nanoporous graphene," *Science Advances*, vol. 5, no. 2, article eaat6951, 2019.

[26] W. Lee, D. Y. Kang, J. Song, J. H. Moon, and D. Kim, "Controlled unusual stiffness of mechanical metamaterials," *Scientific Reports*, vol. 6, no. 1, article 20312, 2016.

[27] X. Zheng, H. Lee, T. H. Weisgraber et al., "Ultralight, ultrastiff mechanical metamaterials," *Science*, vol. 344, no. 6190, pp. 1373–1377, 2014.

[28] F. Zhang, M. Wei, V. V. Viswanathan et al., "3D printing technologies for electrochemical energy storage," *Nano Energy*, vol. 40, pp. 418–431, 2017.

[29] X. Su, X. Li, C. Y. A. Ong et al., "Metallization of 3D printed polymers and their application as a fully functional water-splitting system," *Advanced Science*, vol. 6, no. 6, article 1801670, 2019.

[30] X. Xu, S. Xiao, H. J. Willy et al., "3D-printed grids with polymeric photocatalytic system as flexible air filter," *Applied Catalysis B: Environmental*, vol. 262, article 118307, 2020.

[31] F. Kotz, K. Arnold, W. Bauer et al., "Three-dimensional printing of transparent fused silica glass," *Nature*, vol. 544, no. 7650, pp. 337–339, 2017.

[32] C. H. J. Kim, D. Zhao, G. Lee, and J. Liu, "Strong, machinable carbon aerogels for high performance supercapacitors," *Advanced Functional Materials*, vol. 26, no. 27, pp. 4976–4983, 2016.

[33] X. Xu, J. Zhou, D. H. Nagaraju et al., "Flexible, highly graphitized carbon aerogels based on bacterial cellulose/lignin: catalyst-free synthesis and its application in energy storage devices," *Advanced Functional Materials*, vol. 25, no. 21, pp. 3193–3202, 2015.

[34] F. Zhang, Y. Feng, M. Qin et al., "Stress controllability in thermal and electrical conductivity of 3D elastic graphene-crosslinked carbon nanotube sponge/polyimide nanocomposite," *Advanced Functional Materials*, vol. 29, no. 25, article 1901383, 2019.

[35] X.-L. Wu, T. Wen, H.-L. Guo, S. Yang, X. Wang, and A. W. Xu, "Biomass-derived sponge-like carbonaceous hydrogels and aerogels for supercapacitors," *ACS Nano*, vol. 7, no. 4, pp. 3589–3597, 2013.

[36] T. Zhai, F. Wang, M. Yu et al., "3D MnO_2-graphene composites with large areal capacitance for high-performance asymmetric supercapacitors," *Nanoscale*, vol. 5, no. 15, pp. 6790–6796, 2013.

[37] C. Zhu, L. Yang, J. K. Seo et al., "Self-branched α-MnO_2/δ-MnO_2 heterojunction nanowires with enhanced pseudocapacitance," *Materials Horizons*, vol. 4, no. 3, pp. 415–422, 2017.

[38] B. Yao, L. Huang, J. Zhang et al., "Flexible transparent molybdenum trioxide nanopaper for energy storage," *Advanced Materials*, vol. 28, no. 30, pp. 6353–6358, 2016.

[39] Y. He, W. Chen, X. Li et al., "Freestanding three-dimensional graphene/MnO_2 composite networks as ultralight and flexible supercapacitor electrodes," *ACS Nano*, vol. 7, no. 1, pp. 174–182, 2012.

[40] X. Zhang, J. Luo, P. Tang et al., "A universal strategy for metal oxide anchored and binder-free carbon matrix electrode: a supercapacitor case with superior rate performance and high mass loading," *Nano Energy*, vol. 31, pp. 311–321, 2017.

[41] T. Liu, Z. Zhou, Y. Guo, D. Guo, and G. Liu, "Block copolymer derived uniform mesopores enable ultrafast electron and ion transport at high mass loadings," *Nature Communications*, vol. 10, no. 1, pp. 675–685, 2019.

[42] L. Ma, R. Liu, H. Niu, F. Wang, L. Liu, and Y. Huang, "Freestanding conductive film based on polypyrrole/bacterial cellulose/graphene paper for flexible supercapacitor: large areal mass exhibits excellent areal capacitance," *Electrochimica Acta*, vol. 222, pp. 429–437, 2016.

[43] C. Chen, Y. Zhang, Y. Li et al., "All-wood, low tortuosity, aqueous, biodegradable supercapacitors with ultra-high capacitance," *Energy & Environmental Science*, vol. 10, no. 2, pp. 538–545, 2017.

[44] Y. Song, T. Liu, B. Yao et al., "Ostwald ripening improves rate capability of high mass loading manganese oxide for supercapacitors," *ACS Energy Letters*, vol. 2, no. 8, pp. 1752–1759, 2017.

[45] H. Wang, C. Xu, Y. Chen, and Y. Wang, "MnO_2 nanograsses on porous carbon cloth for flexible solid-state asymmetric supercapacitors with high energy density," *Energy Storage Materials*, vol. 8, pp. 127–133, 2017.

[46] C. Zhu, C. Guan, D. Cai et al., "Carbon nanoarrays embedded with metal compounds for high-performance flexible supercapacitors," *Batteries & Supercaps*, vol. 3, no. 1, pp. 93–100, 2019.

[47] C. Guan, A. Sumboja, H. Wu et al., "Hollow CoO_4 nanosphere embedded in carbon arrays for stable and flexible solid-state zinc-air batteries," *Advanced Materials*, vol. 29, no. 44, article 1704117, 2017.

[48] X. Lu, M. Yu, G. Wang et al., "H-TiO_2@MnO_2//H-TiO_2@C core-shell nanowires for high performance and flexible asymmetric supercapacitors," *Advanced Materials*, vol. 25, no. 2, pp. 267–272, 2013.

[49] L. Dong, C. Xu, Y. Li et al., "Simultaneous production of high-performance flexible textile electrodes and fiber electrodes for wearable energy storage," *Advanced Materials*, vol. 28, no. 8, pp. 1675–1681, 2016.

[50] T. S. Tran, K. M. Tripathi, B. N. Kim et al., "Three-dimensionally assembled graphene/α-MnO_2 nanowire hybrid hydrogels for high performance supercapacitors," *Materials Research Bulletin*, vol. 96, pp. 395–404, 2017.

[51] X. Xiao, T. Ding, L. Yuan et al., "WO_{3-x}/MoO_{3-x}core/shell nanowires on carbon fabric as an anode for all-solid-state asymmetric supercapacitors," *Advanced Energy Materials*, vol. 2, no. 11, pp. 1328–1332, 2012.

[52] X. Tang, C. Zhu, D. Cheng et al., "Architectured leaf-inspired $Ni_{0.33}Co_{0.66}S_2$/graphene aerogels via 3D printing for high-performance energy storage," *Advanced Functional Materials*, vol. 28, no. 51, article 1805057, 2018.

[53] L. Yuan, X.-H. Lu, X. Xiao et al., "Flexible solid-state supercapacitors based on carbon nanoparticles/MnO_2 nanorods hybrid structure," *ACS Nano*, vol. 6, no. 1, pp. 656–661, 2011.

[54] W. Zilong, Z. Zhu, J. Qiu, and S. Yang, "High performance flexible solid-state asymmetric supercapacitors from MnO_2/ZnO core–shell nanorods//specially reduced graphene oxide," *Journal of Materials Chemistry C*, vol. 2, no. 7, pp. 1331–1336, 2014.

[55] Z. Qi, J. Ye, W. Chen et al., "3D-printed, superelastic polypyrrole-graphene electrodes with ultrahigh areal capacitance for electrochemical energy storage," *Advanced Materials Technologies*, vol. 3, no. 7, article 1800053, 2018.

[56] X. Lu, Y. Zeng, M. Yu et al., "Oxygen-deficient hematite nanorods as high-performance and novel negative electrodes for flexible asymmetric supercapacitors," *Advanced Materials*, vol. 26, no. 19, pp. 3148–3155, 2014.

[57] P. Yang, Y. Ding, Z. Lin et al., "Low-cost high-performance solid-state asymmetric supercapacitors based on MnO_2 nanowires and Fe_2O_3 nanotubes," *Nano Letters*, vol. 14, no. 2, pp. 731–736, 2014.

[58] L. Zhang, P. Zhu, F. Zhou et al., "Flexible asymmetrical solid-state supercapacitors based on laboratory filter paper," *ACS Nano*, vol. 10, no. 1, pp. 1273–1282, 2016.

[59] G. Wang, H. Wang, X. Lu et al., "Solid-state supercapacitor based on activated carbon cloths exhibits excellent rate capability," *Advanced Materials*, vol. 26, no. 17, pp. 2676–2682, 2014.

[60] C. Zhu, T. Liu, F. Qian et al., "Supercapacitors based on three-dimensional hierarchical graphene aerogels with periodic macropores," *Nano Letters*, vol. 16, no. 6, pp. 3448–3456, 2016.

[61] K. Xiao, L. X. Ding, G. Liu, H. Chen, S. Wang, and H. Wang, "Freestanding, hydrophilic nitrogen-doped carbon foams for highly compressible all solid-state supercapacitors," *Advanced Materials*, vol. 28, no. 28, pp. 5997–6002, 2016.

[62] A. Sumboja, C. Y. Foo, X. Wang, and P. S. Lee, "Large areal mass, flexible and free-standing reduced graphene oxide/manganese dioxide paper for asymmetric supercapacitor device," *Advanced Materials*, vol. 25, no. 20, pp. 2809–2815, 2013.